

Hover Performance Correlation for Full-Scale and Model-Scale Coaxial Rotors



Joon W. Lim*
Research Scientist
Aeroflightdynamics Directorate (AMRDEC)
U.S. Army Research, Development and Engineering Command
Ames Research Center, Moffett Field, CA



Kenneth W. McAlister¹
Research Scientist



Wayne Johnson
Research Scientist
Aeromechanics Branch
National Aeronautics and Space Administration
Ames Research Center, Moffett Field, CA

The hover performance data of full-scale and model-scale coaxial rotors have been compared with CAMRAD II predictions having a free vortex wake analysis. Performance correlations of a coaxial rotor were made with a variation of key parameters including the rotor spacing and height. To understand aerodynamic behavior of the U.S. Army Aeroflightdynamics Directorate (AFDD) coaxial rotor operating over a range of Reynolds numbers from 36,000 to 180,000, the Reynolds number scaling effect was explored using an airfoil design code, MSES. It was found that the coaxial rotor spacing effect on hover performance was minimal for the rotor spacing larger than 20% of the rotor diameter. The measured performance data showed that more thrust was lost from the lower rotor of a coaxial than the upper rotor due to a larger rotor-to-rotor wake interference effect, and the lower rotor kept only an 81% of the single rotor OGE (out-of-ground effect) thrust whereas the upper rotor maintained a 90%. The lower rotor IGE (in-ground effect) thrust increased quickly by 26% as the rotor approached to the ground from the position of an 80% of the rotor diameter to 10%, and the corresponding IGE power increased by 17%. These thrust and power characteristics were well predicted. Overall, the performance prediction for the coaxial rotor was satisfactory when compared with the measured data.

Nomenclature

C_P	rotor power coefficient
C_T	rotor thrust coefficient
c	chord
c_d	drag coefficient
c_l	lift coefficient
D	rotor diameter
G	rotor height above the ground
K_D	scaling factor for the drag
K_L	scaling factor for the lift
M	Mach number
Re	Reynolds number
r	radial distance from the hub center
r_c	vortex core radius
r_{c0}	initial vortex core radius
S	rotor spacing between two rotors
t_w	wake age in time
ν	kinematic viscosity
α	angle of attack
δ	ν turbulence viscosity parameter

σ	rotor solidity
ζ	azimuthal wake age

Introduction

A recent announcement by Sikorsky Aircraft Corporation of their intent to build and test the X2 Technology Demonstrator (Refs. 1–3) and the Baldwin Technology Company's proposal for the coaxial Mono Tiltrotor (Ref. 4), in conjunction with a rising interest in heavy lift helicopters, has led to a renewed interest in coaxial rotor configurations. The concept of a coaxial rotor system is not new, but little work has been done in the decades since Sikorsky's application of the Advancing Blade Concept (ABC) Demonstrator (Refs. 5–7), and, in Russia, the Kamov Company's successful development of coaxial rotor configurations into a series of production helicopter models, including the Ka-27 and Ka-50 helicopters.

The objective of the present work is to explore hover performance for both full-scale and model-scale coaxial rotors, using a comprehensive rotorcraft analysis tool having a free wake analysis as an extension of the work completed in Ref. 8. The results will help in better understanding the effect of coaxial rotor wake interference on performance, and additionally will assess the analytical capability of coaxial rotor performance modeling.

Reference 9 provides a comprehensive survey of the major aerodynamic experiments and computational models dealing with coaxial rotor

*Corresponding author; email: joon.lim@us.army.mil.

Presented at the American Helicopter Society 63rd Annual Forum, Virginia Beach, VA, May 1–3, 2007. Manuscript received June 2007; accepted April 2009.

¹Currently retired.

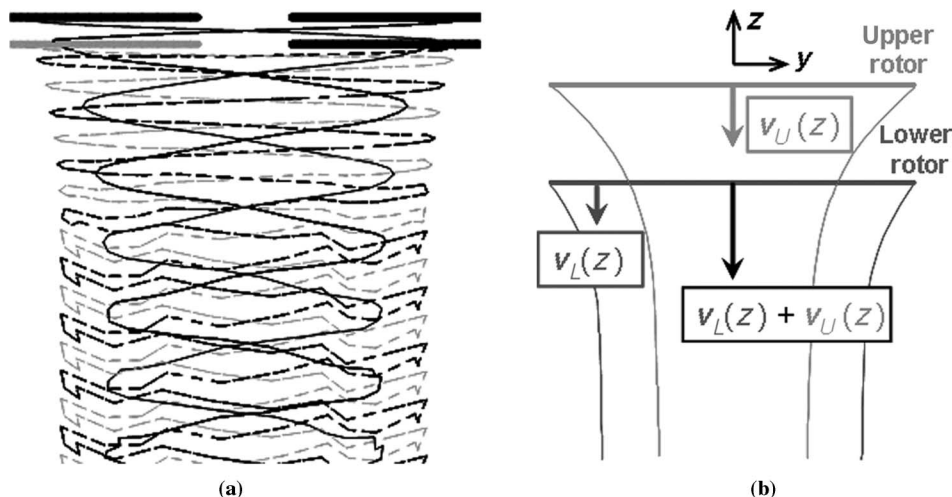


Fig. 1. Free tip vortex wake for a Harrington coaxial rotor. (a) Computed tip vortex geometries. (b) Sketch of simplified rotor wake velocities.

systems during the last half of the twentieth century. It addresses issues such as rotor spacing, load sharing between the rotors, and wake structures, and also discusses in great detail the research from the international rotorcraft community for a coaxial rotor.

References 10 and 11 demonstrated that a free wake analysis was able to capture the basic physics of the coaxial rotor wake problem. The coaxial rotor correlation efforts made further progress with an application of the computational fluid dynamics methodology (Refs. 12,13) to show good correlation of the coaxial rotor performance data.

Reference 8 examines the hover performance of a small-scale generic tilt rotor in both single and coaxial rotor [the U.S. Army Aeroflight-dynamics Directorate (AFDD) rotor]. The key coaxial rotor parameters that were varied in the test included the rotor height and spacing. An analytical model, based on the blade element theory with induced velocities experimentally calibrated for a coaxial rotor, was also presented, but showed a limited correlation.

This paper compares correlation results achieved in three rotor configurations: the Harrington rotor (Ref. 14), an XH-59A (Refs. 5–7), and an AFDD coaxial rotor (Ref. 8). Ground and rotor spacing effects are investigated, and a Reynolds number scaling effect is explored in depth for the AFDD coaxial rotor.

Harrington Rotor Performance

A full-scale, experimental investigation of the coaxial rotor hover performance was carried out by Harrington in the Langley full-scale tunnel in 1951 (Ref. 14). Two different rotor blade planforms (Rotor 1 and Rotor 2) were tested in the coaxial rotor configuration, each with a different airfoil thickness and chord variation on the blade. Each rotor had two untwisted blades with 25-ft diameter.

The Rotor 1 chord was tapered with a taper ratio of 0.35 from root to tip. The airfoil thickness was nonlinearly tapered from the root (31% chord) to the tip (12% chord). Finally, Rotor 1 had a solidity of 0.027 (as a coaxial, 0.054), with the rotor spacing of 9.3% of the rotor diameter.

Rotor 2 had wider but constant-chord blades with a solidity of 0.076 (as a coaxial, 0.152). The blades were linearly tapered in thickness (31% chord at root to 15% at tip). The rotor spacing for Rotor 2 was 8.0% of the rotor diameter. Static-thrust performance data were available for both the single and coaxial rotor systems. The Reynolds number at the 75%

blade span ranged from 0.8 million to 1.3 million for Rotor 1 and from 1.9 million to 2.8 million for Rotor 2.

Figure 1(a) shows the tip vortex free wake geometry predicted by CAMRAD II for the Harrington coaxial rotor configuration. The tip vortex geometry from the upper rotor contracts into the lower rotor so that its wake structure convects through and below the lower rotor. The axial displacement of the upper rotor helicoidal (inner) wake is more than twice the lower rotor (outer) wake axial displacement. This is due to a coaxial rotor wake interaction. The inner helicoidal wake is convected downstream with the downwash velocities added from the upper and lower rotors when it is positioned below the lower rotor. The outer helicoidal wake is convected with the downwash velocity of the lower rotor without a significant rotor wake interaction. Figure 1(b) is a sketch of simplified wake velocities of a coaxial rotor, illustrating how the inflow velocities of the upper and lower rotors vary with the vertical position. It is interesting to observe that the upper and lower rotor wake geometries remained distinct, which is consistent with the observations made from Ref. 15.

Correlation of the thrust-to-power (power polar) and figure of merit (*FM*) are shown in Fig. 2 for the Harrington Rotor 1. The definition of *FM* used in this study is

$$FM_{\text{coax}} = \frac{(C_{T,U} + C_{T,L})^{3/2}}{\sqrt{2}(C_{P,U} + C_{P,L})} \quad (1)$$

where the subscripts *U* and *L* indicate the upper and lower rotors, respectively. The measured data are represented by the symbols in the figure, whereas the CAMRAD II (Ref. 16) predictions are given by the lines. The predicted Rotor 1 performance polar is well correlated with the test data. Below $C_T = 0.003$, the coaxial rotor requires more power than the single rotor, because of energy loss possibly due to wake interactions between the two rotors of a coaxial. As the C_T increases above 0.003, the single rotor would experience a stall and require more power than a coaxial rotor. *FM* is well predicted below a thrust level (C_T/σ) of 0.10, with a coaxial rotor showing higher *FM* than a single rotor. Note that the solidity of a coaxial rotor (σ_{coax}) is 2σ .

A similar comparison was applied to the Harrington Rotor 2. Figure 3 shows the power polar correlation for Rotor 2. This rotor had rectangular blades with a solidity (σ) approximately three times greater than Rotor 1. The performance predictions are equally as good as in Rotor 1, and the *FM* is also well predicted.

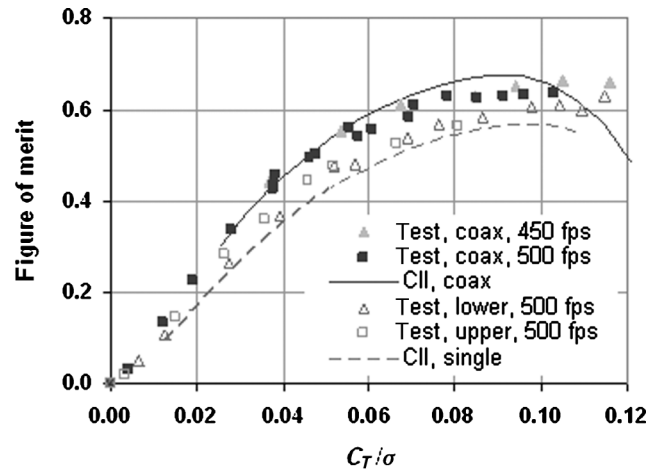
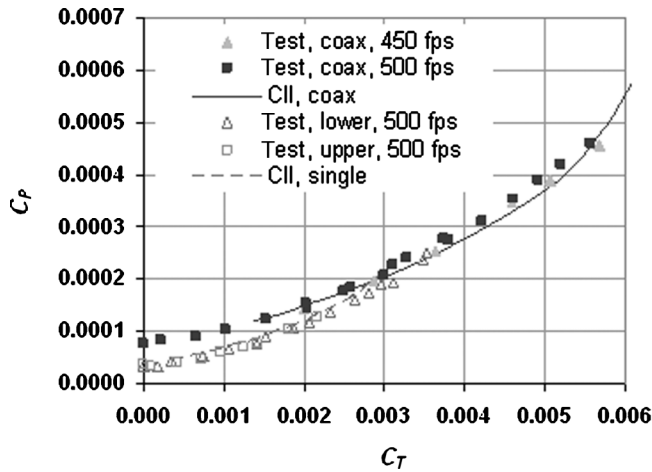


Fig. 2. Prediction of hover performance for Harrington Rotor 1 (coaxial solidity = 0.054).

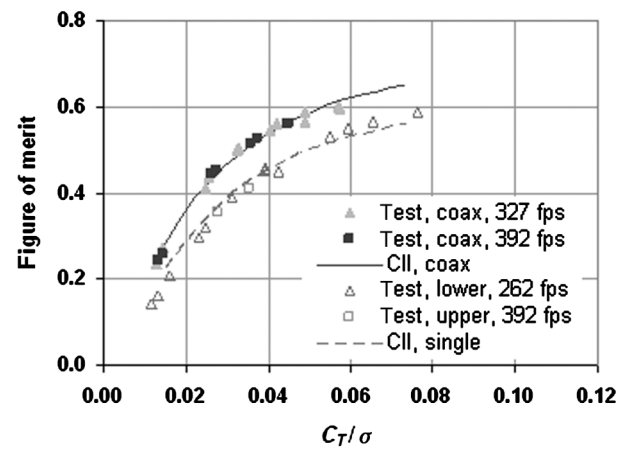
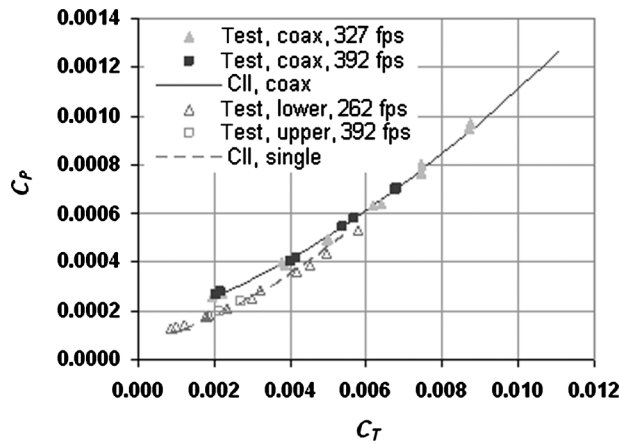


Fig. 3. Prediction of hover performance for Harrington Rotor 2 (coaxial solidity = 0.152).

XH-59A Helicopter Performance

A flight test of the XH-59A ABC demonstration helicopter was reported in Refs. 5–7. The aircraft featured a coaxial, hingeless rotor system with a rotor solidity of 0.127 (as a coaxial, 0.254). Each rotor had three 18-ft-long blades with a 10-deg twist rate. The hover performance data, with and without ground effect, were

measured during the flight for wheel heights of 10, 20, 35, and 75 ft.

Figure 4 shows correlation of the out-of-ground effect (OGE) hover performance data for the XH-59A flight. The flight test data were obtained from flights 6 and 10 weighing 9900–10,700 lb, with the tip Mach numbers ranging from 0.54 to 0.58. Note that the flight test data represent only the coaxial rotor contribution after subtracting the performance

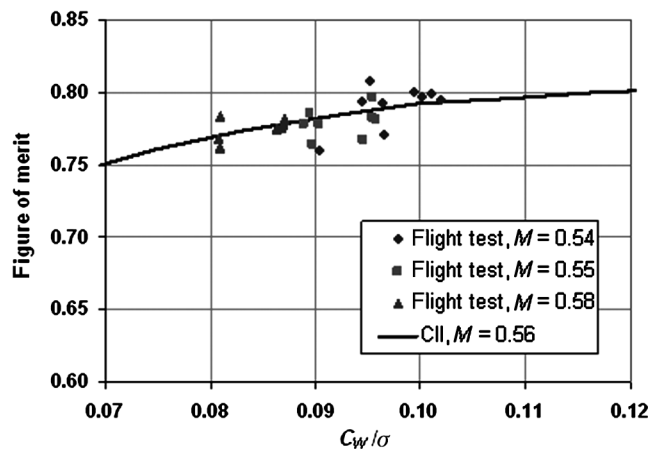
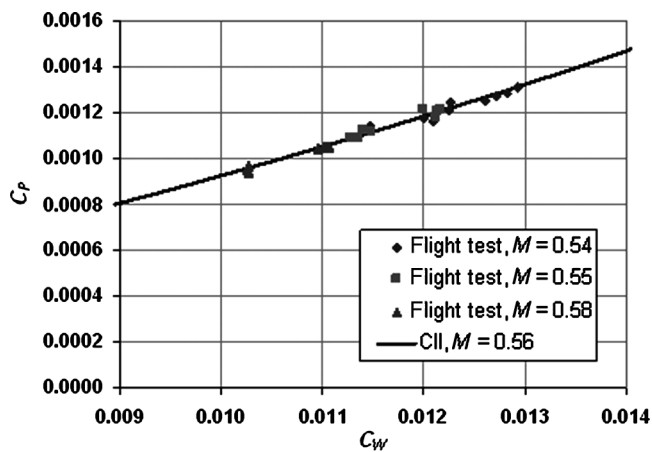


Fig. 4. Prediction of OGE hover performance for XH-59A.

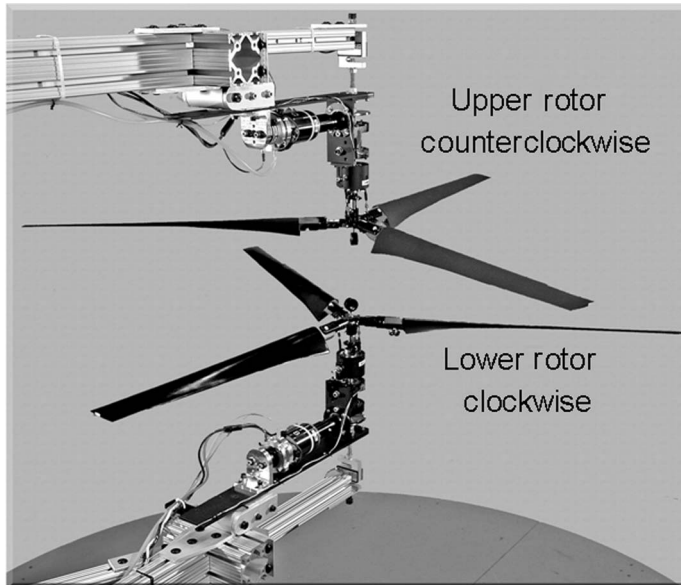


Fig. 5. AFDD coaxial rotor setup.

losses due to the fuselage and the drive train system. It was estimated in Ref. 6 that the download on the fuselage would be 6% of the coaxial rotor thrust, and that the transmission and accessory losses would be 75 hp. The predicted power polar matches well with the flight test data. A large scatter of the *FM* data is observed, ranging from 0.75 to 0.80, and the *FM* is satisfactorily predicted.

AFDD Coaxial Rotor Performance

A small-scale, hover performance test of the AFDD coaxial rotor was conducted in 2005 by McAlister et al. (Ref. 8) in a closed 21 × 23 × 16-ft laboratory at Ames Research Center. This AFDD coaxial rotor test setup is shown in Fig. 5. The rotors were tested in both coaxial and single rotor configurations. The two (upper and lower) rotors and their test stands were shown to be nearly identical so that each rotor could be

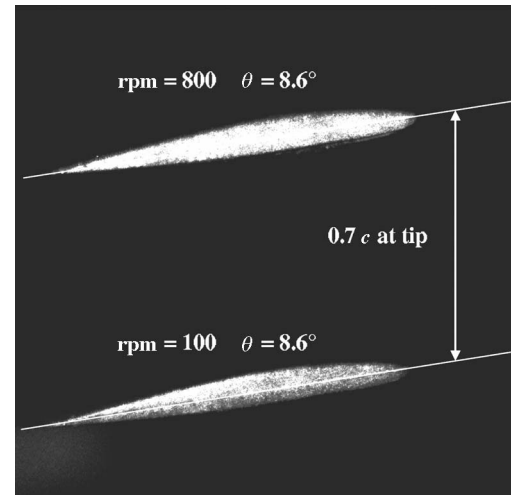


Fig. 7. Measured flap tip deflections at 100 and 800 rpm ($\theta_{tip} = 8.6^\circ$, $\theta_{75} = 15.1^\circ$).

separately evaluated. The upper rotor rotated counterclockwise, whereas the lower rotor rotated clockwise when viewed from the top. Each rotor was a small-scale, three-bladed, generic tilt rotor (similar to the XV-15) operating at a nominal rotor speed of 800 rpm. The rotor blade had a 4.05-ft diameter with a solidity of 0.0784. Note that the coaxial solidity (2σ) was 0.1568. The blade had a constant chord of 2 inches except near the blade grip region where the chord was slightly larger.

Figure 6 shows the airfoil and twist distribution of the AFDD coaxial rotor blade planform. The airfoil sections varied nonlinearly in thickness along the blade span, utilizing the XV-15 airfoil coordinates. They consisted of the 64-series, five-digit airfoils from 8% thickness at the tip to 32% thickness at the root. The hover tip Mach number was 0.15 at a nominal speed of 800 rpm, with the Reynolds numbers ranging from 36,000 at the root to 180,000 at the tip for this operating speed. The total nonlinear blade twist was 37° . The blade twist was defined as zero at the 75% blade span location.

The blade was considered torsionally rigid but showed significant elastic coning. Figure 7 shows the images of the deflected blade tips

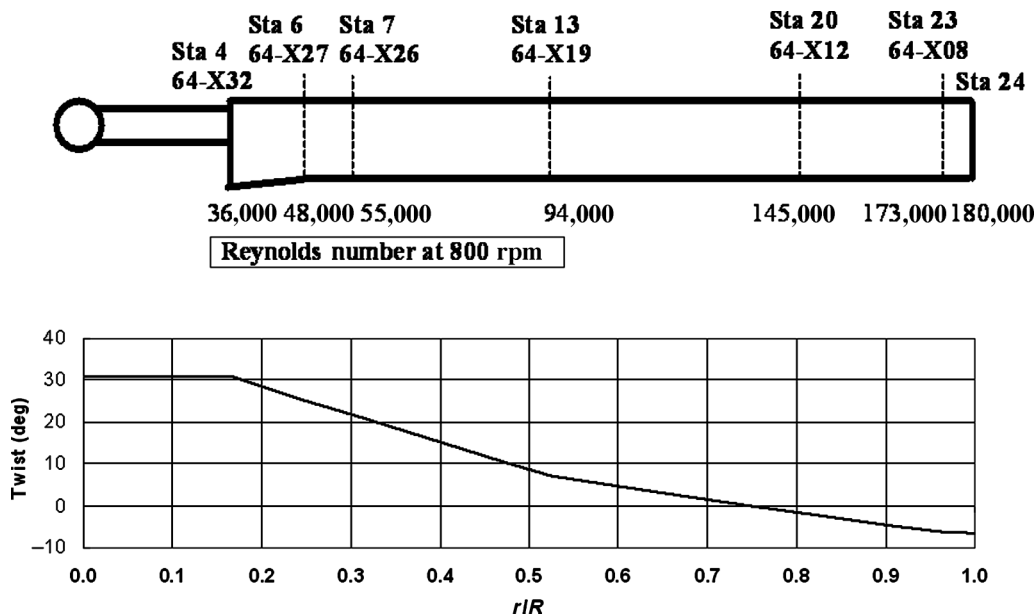


Fig. 6. Airfoil sections and twist distribution of the AFDD coaxial blade.

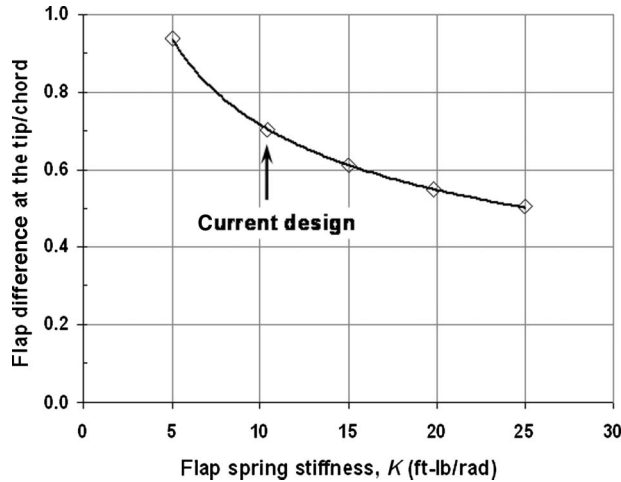


Fig. 8. Computed flap difference at the blade tip between 100 and 800 rpm with a flap spring stiffness variation ($\theta_{75} = 15.1^\circ$).

illuminated by a YAG laser when the operating speed was changed from 100 to 800 rpm with a collective pitch of 15.1° . The difference of the measured flap tip deflections between these two operating speeds was 0.7 chords. This elastic coning effect was modeled by introducing a flap spring located at 1 inch from the hub center in the blade span. Figure 8 shows the computed difference of the flap tip deflection between 100 and 800 rpm with a flap spring stiffness variation, and the estimated flap spring stiffness is found to be 10.4 ft-lb/rad by matching with the measured difference.

The hover performance data of the AFDD coaxial rotor were measured for a wide range of coaxial rotor geometric variations including both single and coaxial rotor configurations with variations in the rotor height as well as spacing. This data set provides a basis for evaluating coaxial rotor performance with both the ground and rotor-to-rotor interference effects.

Free wake vortex core growth model

The vortex core grows with a wake age. The core growth of a Lamb–Oseen or Squire laminar vortex varies with the square root of a wake age, and adding the turbulent viscosity effect gives the vortex core growth model (Refs. 17–20) as

$$r_c = 2.2418\sqrt{\delta\nu t_w} \quad (2)$$

where r_c is the vortex core radius, δ is a turbulent viscosity parameter, ν is a kinematic viscosity coefficient, and t_w is a wake age in time. A simple vortex core growth model used in this paper is similar to Eq. (2) based on the square root of an azimuthal wake age ζ as

$$\frac{r_c}{c} = \frac{r_{c0}}{c} + \sqrt{\frac{\zeta}{k \cdot 2\pi}} \quad (3)$$

This core model adds an initial core radius (r_{c0}) at zero wake age, with a scaling factor k determining how fast the vortex core grows with a wake age. For the computation, the core growth model was set to grow by one chord length in three rotor revolutions ($k = 3$) with an initial core radius of 5% chords. Although it was at least one order of the magnitude smaller than the measured vortex core growth data reported in Ref. 21, this k value made no significant effect on the sensitivity of the results in the hover performance prediction.

Table 1. Comparison of Reynolds and Mach numbers at the tip in hover

	M_{tip}	Re_{tip}
AFDD coaxial	0.15	180,000
XV-15	0.65	5,700,000

Reynolds number correction

As interests in microaerial vehicles grow, the size of the rotor becomes smaller, and a Reynolds number effect becomes correspondingly more significant. The size of the AFDD coaxial rotor (Ref. 8) was approximately a 1/6-scale of the XV-15 rotor (Ref. 22). Table 1 compares both Reynolds and Mach numbers at the tip in hover for the small-scale AFDD coaxial and the full-scale XV-15 rotor. Since the tip Mach number of the AFDD rotor is 0.15, the flow field in the entire rotor is considered incompressible. Note that the tip Reynolds number of the AFDD coaxial rotor is only 3% of the full-scale XV-15 rotor value. To account for the rotor-scaling effect, a Reynolds number correction (Ref. 23) can be applied for the lift and drag coefficients such that

$$\begin{aligned} c_l &= K_L c_{l,2d}(\alpha/K_L) \\ c_d &= \frac{1}{K_D} c_{d,2d} \end{aligned} \quad (4)$$

where $K_i = (Re/Re_i)^n$, $i = L$ or D and Re_i is the Reynolds number at which the airfoil table was generated. The value of the exponent n is selected for the best curve-fit with the measured data. For a fully turbulent flow, n is 0.125–0.20, roughly based on the one-fifth power law. For a laminar separated flow, n is 0.4–0.5, roughly based on the one-half power law. A constant drag could be added to the airfoil table to take into account any unknown discrepancies of power prediction.

MSES-based airfoil table

The information for Reynolds number, Re_i , is not generally included in an airfoil table, where Mach numbers are incrementally defined in the range of 0–1 with an angle-of-attack variation. The airfoil table data for the full-scale rotors are generally considered unchanged below a Mach number of 0.3 due to the incompressible flow condition. These airfoil tables likely represent the flow field at a reasonably high Reynolds number in the order of several millions at the blade tip.

Airfoil tables can be alternatively generated based on accurate Reynolds numbers by using the MSES (Ref. 24) code. The MSES code uses compressible Euler equations to solve the inviscid flow field, coupled with suction and pressure solutions of a viscous boundary layer. The boundary layer transition location is determined via the amplitude ratio method (e^n) using growth rates that are precomputed from solutions of the Orr–Sommerfeld equation (Ref. 25). The proper critical amplification parameter, n_{crit} , can be empirically determined based on the measured data of the boundary layer transition and pressure for an airfoil. In this study, the standard value ($=9$) for the MSES code was used for n_{crit} without sufficient validation due to a lack of the available data. Note that MSES exhibited difficulty achieving a numerical convergence of the viscous flow field solution when the freestream Mach number was below 0.10.

The MSIS code is a part of the MSES software package and functionally equivalent to the MSES code, except that it solves the entropy-conserving Euler equation by imposing the isentropic condition everywhere, whereas MSES solves the streamwise momentum-conserving

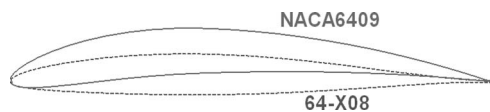


Fig. 9. A comparison of airfoil coordinates between NACA 6409 and 64-X08.

Euler equation. It is reported in Refs. 24 and 25 that MSIS is capable of calculating the flow field for extremely low freestream Mach numbers.

MSES code validation. Experimental airfoil data at very low Reynolds numbers are available, but are mostly used with thin airfoils suited for radio-controlled (RC) sailplanes. Reference 26 provides a collection of experimental data for numerous RC sailplane airfoils at Reynolds number of 60,000–300,000. The wind tunnel wing models were built by many experienced model sailplane enthusiasts for the data measurement, and the airfoil performance data were measured for a total of 53 airfoils ranging in thickness from 8% to 15% and in camber from 0% to 6%. The freestream velocity was very low during the wind tunnel testing in order to have this range of Reynolds numbers, and the wing models had a relatively large chord of 1 ft.

The NACA 6409 airfoil was used for validation of the MSES/MSIS code (Ref. 24), which appeared a challenging task due to its high airfoil camber in the airfoil database (Ref. 26). Figure 9 compares the NACA 6409 airfoil coordinate with the 64-X08 airfoil. This NACA airfoil had a 9% thickness with a 6% camber. The 64-X08 airfoil was used for the blade tip region of the AFDD coaxial as shown in Fig. 6 and expected to have a Reynolds number in the range of 160,000–180,000. So, the operating condition for NACA 6409 was set to be in the neighborhood of these Reynolds numbers, and the predicted lift is compared in Fig. 10 with the test data. The measured zero-angle-of-attack lifts are not small due to its high camber. The predictions appear slightly higher by 0.04 at $Re = 103,000$, but good at $Re = 200,000$. The lift slopes are predicted higher at both Reynolds numbers. The lift comparison at $Re = 200,000$ indicates that the airfoil may experience stall at angles of attack lower than the predicted value.

The airfoil performance polar for NACA 6409 is compared in Fig. 11 at Reynolds numbers of 79,000, 103,000, 147,000, and 200,000. At $Re = 79,000$, the drag value at the drag bucket is underpredicted by 0.004, and these MSES underpredictions are gradually improved at higher Reynolds numbers. At $Re = 200,000$, the drag bucket is satisfactorily predicted with MSES, except for the maximum lift as seen in Fig. 10.

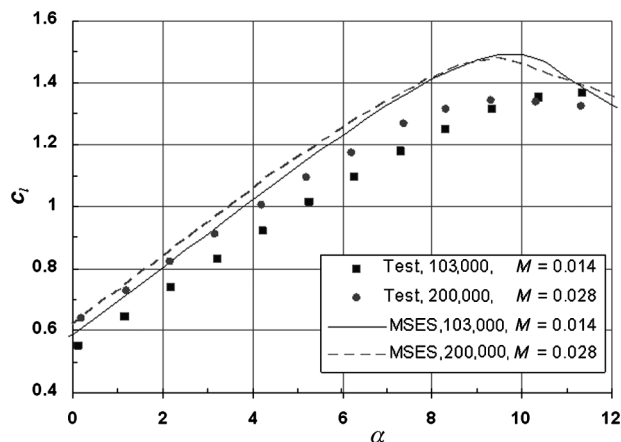


Fig. 10. MSES lift prediction for NACA 6409 for Reynolds numbers of 103,000 and 200,000.

AFDD coaxial airfoil tables generation. The AFDD coaxial airfoil tables generated using the MSES code were suited for the low Reynolds number operating condition. Reynolds numbers were varied from 12,000 to 570,000 to generate airfoil tables for all airfoils, with corresponding Mach numbers ranging from 0.01 to 0.40. Note that the AFDD coaxial had Reynolds numbers in the range of 36,000–180,000 as shown in Fig. 6. A total of six MSES-based C81 tables were generated for the AFDD coaxial rotor computation: 64-X08, 64-X12, 64-X19, 64-X26, 64-X27, and 64-X32 airfoils.

Figure 12(a) compares aerodynamic coefficients of the 64-X12 airfoil at $M = 0.3$ and 0.4 between the MSES result and the XV-15 data. The Reynolds numbers are 355,000 at $M = 0.3$ and 473,000 at $M = 0.4$ for the AFDD coaxial 64-X12, and those for the full-scale XV-15 are 2.5 million at $M = 0.3$ and 3.3 million at $M = 0.4$. The lift coefficients agree satisfactorily between the two rotors despite the difference of Reynolds numbers. However, the drag coefficient for the AFDD coaxial is higher by 0.002 at the drag bucket than the XV-15 data, which is considered due to a lower Reynolds number.

Figure 12(b) compares aerodynamic coefficients with a thicker airfoil. The airfoils used for comparison are 64-X19 for MSES and 64-X18 for XV-15. The Reynolds numbers for both airfoils are the same as in Fig. 12(a). The thick airfoil, 64-X18 or 64-X19, shows a wider drag bucket than the thin airfoil, 64-X12. The results of both thick airfoils (MSES-based 64-X19 and XV-15 64-X18) demonstrate similar trends. The minimum drag of the MSES-based airfoil is higher by 0.003 than that of the XV-15 airfoil due to a Reynolds number effect.

The laminar separation bubble phenomenon (Ref. 26) is a process of laminar separation, transition-to-turbulence, and then turbulence reattachment that may result in a large energy loss. When a laminar flow separates as a result of encountering a steep adverse pressure gradient on the airfoil surface, a laminar bubble is formed that causes a sudden drop in the lift and a sharp increase in the drag. The separated free shear layer becomes unstable, and the free shear flow around the bubble rapidly transitions from a laminar flow to a turbulent flow, then reattaches to the airfoil surface.

MSES/MSIS, having the free boundary layer transition condition, was not always successful in obtaining numerically well-converged solutions. This difficulty was mostly observed from the case computed with MSES in the neighborhood of $M = 0.10$, or using MSIS with a very thick airfoil. So, the boundary layer transition position was consequently constrained to improve this difficulty. Recalling that the hover tip Mach number was 0.15, MSES was used for $0.10 < M < 0.15$, and MSIS was for $M < 0.10$. The boundary layer transition position in MSES/MSIS moves freely within the user-specified maximum bounds when constrained.

The maximum boundary layer transition bounds in MSES were set at 0.40 chords for suction and 0.60 chords for pressure, which is applicable for all airfoils. The transition bound in MSIS varied for different airfoils. For X08 and X12, the transition bounds were specified as 0.80–0.90 chords for both the suction and pressure, depending upon the Mach number. For a thicker airfoil, the transition bound was specified such that it slowly moved forward from the value for a thin airfoil. For X19, the transition bound was in the range of 0.70–0.75, and for X26 and X27 it was in the range of 0.60–0.70. For X32, the flow could be very turbulent and the transition bound was set in the range of 0.40–0.70. Note that the transition input of 1.0 chord implies that the transition position can be anywhere in the airfoil coordinate, which is called a free transition.

Figure 13 shows a performance polar computed using MSES for the 64-X12 and 64-X19 airfoils. The 64-X12 airfoil was located at the 81% blade span, operating with Reynolds numbers in the neighborhood of 94,000–173,000. Similarly, the 64-X19 airfoil was at 53% span, operating in the range of Reynolds numbers of 55,000–145,000. The 64-X12 performance polar exhibits a smooth trend for $Re = 118,000$ or higher,

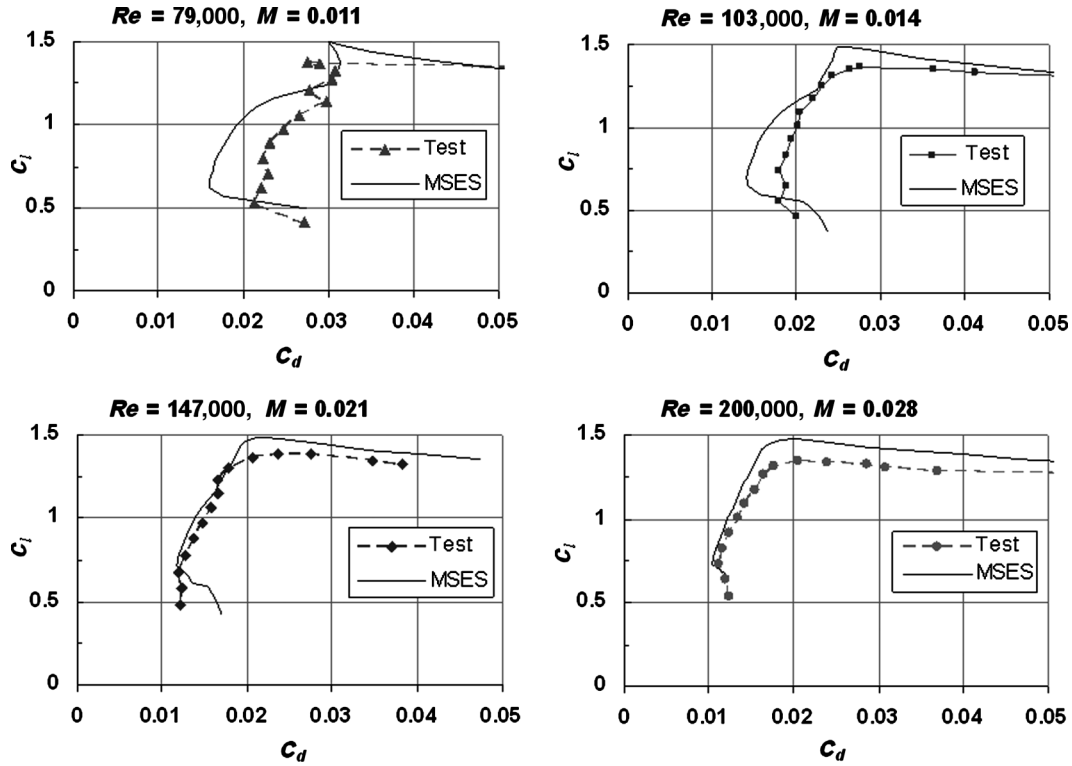


Fig. 11. Correlation of NACA 6409 airfoil performance for Reynolds numbers from 79,000 to 200,000.

but begin to show a large drag rise at $Re = 95,000$ which could be resulted from a laminar separation bubble. The 64-X19 airfoil appears to exhibit a laminar separation bubble at an even higher Reynolds number due to its higher airfoil thickness. At $Re = 142,000$, this X19 airfoil flow field appears normal, but at $Re = 118,000$ or below the drag rises substantially due to a laminar separation.

Three-dimensional rotation effect on flow separation

The three-dimensional (3D) rotation effect on the boundary layer produces a delay of flow separation or stall, particularly for the inboard sections of rotating blades (Refs. 27,28). Separated flow on the airfoil surface stretches outward in the radial direction due to rotor spinning,

which results in thinner boundary layer thickness and delay in flow separation or stall. Such separation delay in the 3D flow field can be modeled using an empirical correction to the airfoil coefficients in the two-dimensional table. This lift correction, which is due to the 3D rotation effect, is based on the following formulation given in Ref. 27:

$$K_L = \left[\frac{c/r}{0.136} \left(\frac{0.1517}{c/r} \right)^{1/1.084} \right]^n \tag{5}$$

$$= [1.291(c/r)^{0.0775}]^n$$

where c is the blade chord and r is the radial distance from the center of rotation. The exponent, n , is varied from 0.8 to 1.8, with the larger

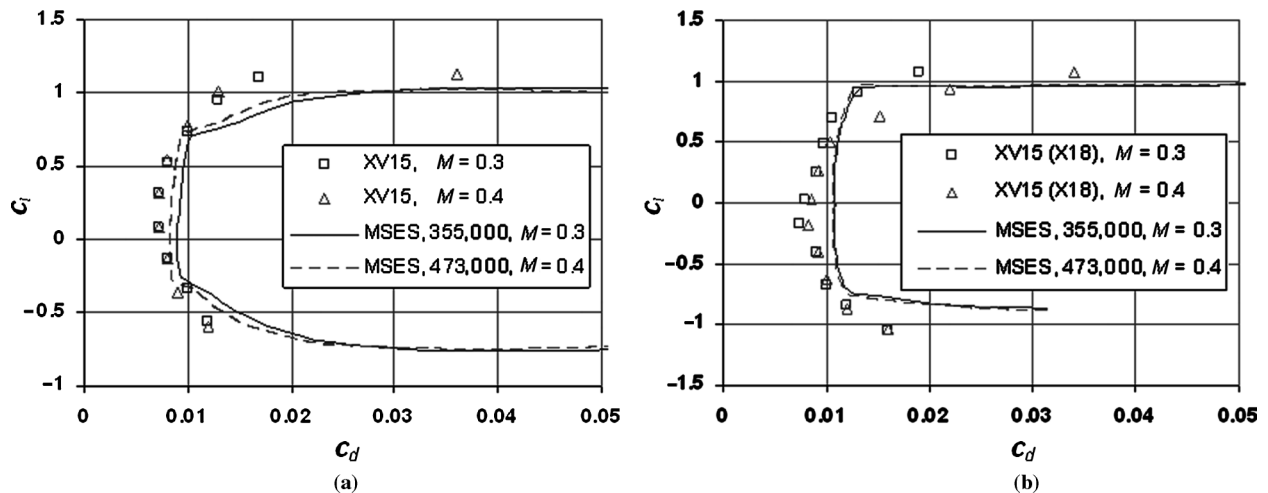


Fig. 12. Comparison of airfoil performance between the XV-15 tables and the MSES predictions. (a) 64-X12 airfoil. (b) 64-X19 airfoil.

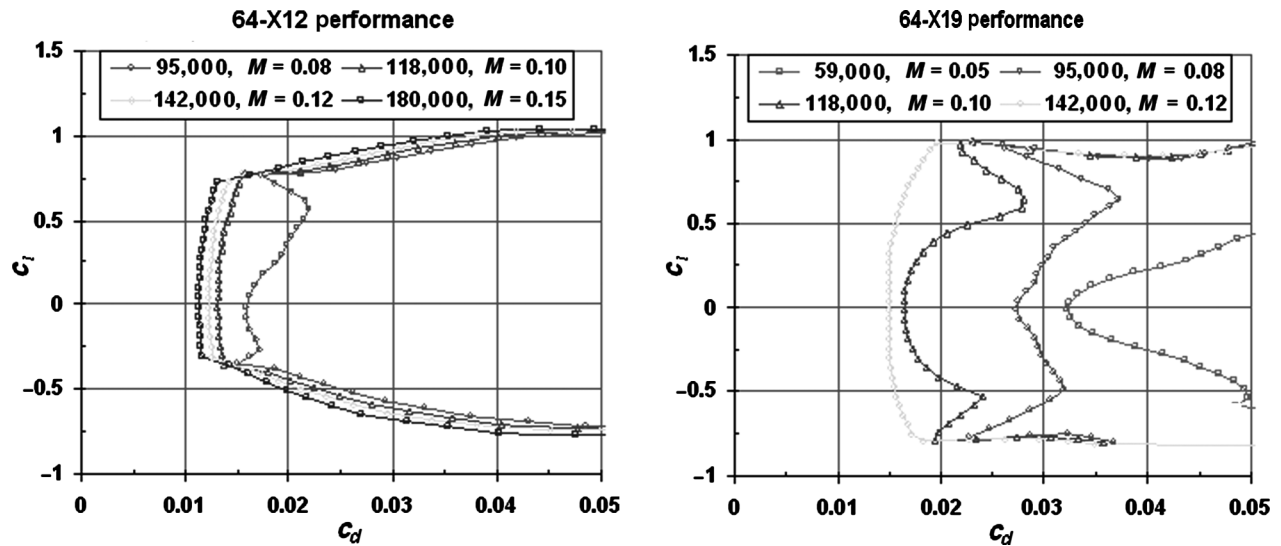


Fig. 13. Predicted performance of 64-X12 and 64-X19 airfoils computed using MSES at low Reynolds numbers.

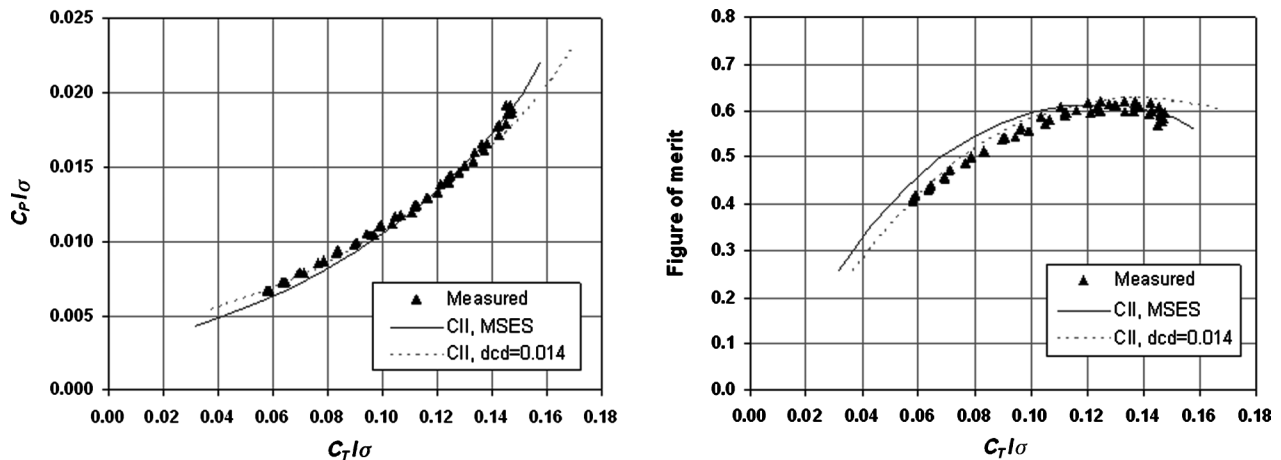


Fig. 14. Correlation of the power level and the *FM* for the AFDD single rotor at 800 rpm.

values typically giving better correlation. This predetermined lift scaling factor, K_L will be substituted in Eq. (4).

AFDD single rotor performance

Thrust and power. A correlation of performance and *FM* for the AFDD single rotor is presented in Fig. 14. The lower rotor of the AFDD coaxial was used for the single rotor comparison unless otherwise stated. The AFDD rotor operated at a nominal speed of 800 rpm with the hover tip Mach number of 0.15. The measured data are depicted as symbols in the figure. The CAMRAD II predictions were made with (1) MSES-based airfoil tables and (2) XV-15 airfoil tables with adding a constant drag ($\Delta c_d = 0.014$). Since the tip Reynolds number of the AFDD coaxial was only 3% of the full-scale XV-15, the Reynolds number scaling effect would be substantial. A free wake analysis was used for the prediction, and the initial vortex core radius was chosen as 5% chords. The vortex core growth was set to grow by one chord length in three rotor revolutions. The 3D rotation effect was included with an exponent, $n = 1.8$, in Eq. (5). As seen in Fig. 14, both approaches capture reasonably the overall trend of the measured data. At a low thrust level, an approach of adding a constant drag works better compared with the MSES-based

tables. At a thrust level (C_T/σ) of 0.14 or higher, the rotor may undergo stall or separation, where the MSES approach is shown more effective. The same trend is repeated in the *FM* prediction. Better predictions with MSES-based tables at a higher thrust level may result from an improved blade stall prediction with accurate airfoil tables.

Figure 15 shows the 3D rotation effect on the power polar. The prediction with no 3D rotation effect exhibits the stall at a lower thrust level, which requires a higher power. Figure 16 shows a breakdown of the predicted power computed by using the MSES-based tables. The induced power (C_{Pi}) increases with a thrust level increase, whereas the profile power (C_{Po}) remains constant at a lower thrust level and then begins to rise near the stall.

Rpm sweep. The Reynolds number effect becomes more significant as the rotor rpm lowers. In such cases, a correction may be necessary in two ways: a simple correction as given by the expression in Eq. (4), or generating airfoil tables based on accurate Reynolds numbers using MSES. The AFDD coaxial performance prediction using existing XV-15 airfoil tables requires a Reynolds number correction since those tables were generated based on the full-scale rotor operating conditions. The best performance prediction using a simple Reynolds number correction

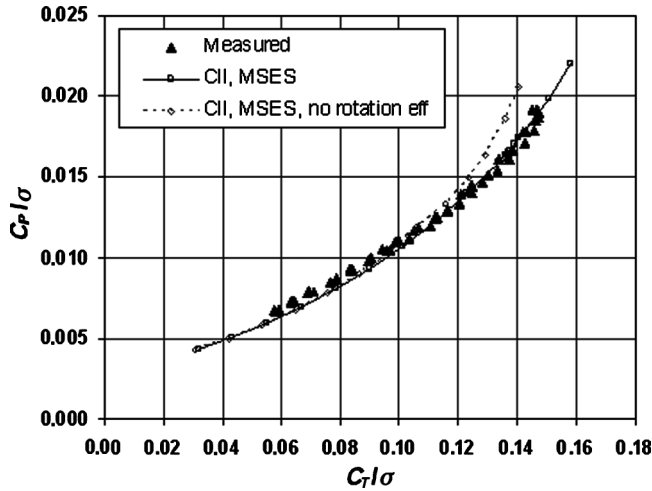


Fig. 15. Correlation of the power level for the AFDD single rotor at 800 rpm with and without the 3D rotation effect.

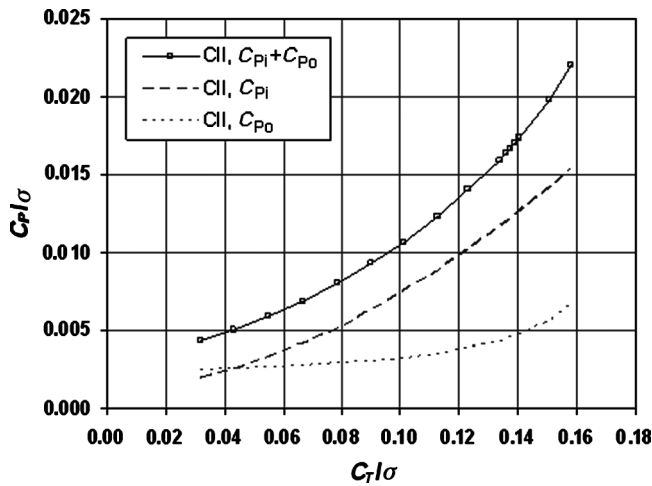
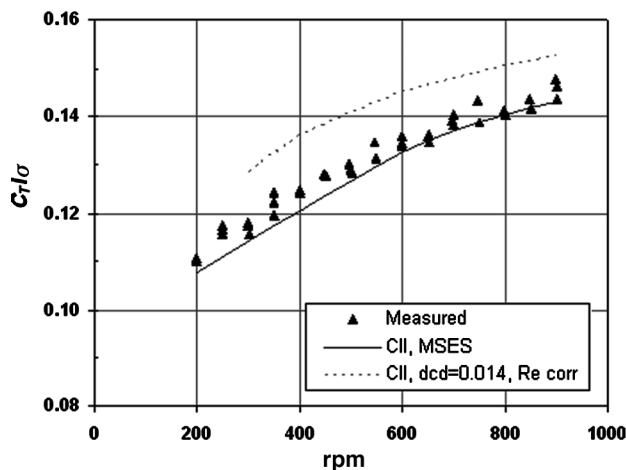


Fig. 16. A breakdown of the computed power level for the AFDD single rotor at 800 rpm.



for an AFDD coaxial was found by letting $n = 0.4$ for K_L and $n = 0.5$ for K_D in Eq. (4) at a nominal operating speed of 800 rpm.

Figure 17 correlates the thrust and power levels with a rpm sweep for the AFDD single rotor. The predictions were made using two approaches: (1) the MSES-based tables and (2) the XV-15 tables with a simple Reynolds number correction as well as adding a constant drag (the Δc_d approach). The collective pitch of the rotor was set 15.2° . As the rpm was reduced from a nominal speed of 800 to 200 rpm, the tip Reynolds number decreased from 180,000 to 45,000, and so the Reynolds number effect became significant. The measured data indicated that the Reynolds number effect resulted in a decrease in the thrust level by 27% and an increase in the power level by 15% with a rpm change from 800 to 200 rpm. The constant drag approach (Δc_d) showed a similar trend of the thrust and power levels to the measured data but overpredicted them approximately by 7%. These correlations were significantly improved with the MSES-based tables.

Ground effect. The ground effect was modeled by the method of images (Refs. 15, 29) that creates a mirror image of the rotor wakes above and below the ground plane. Figure 18 shows the AFDD single rotor ground effect on the thrust and power levels with two different collectives. The rotor height (G) is defined as the rotor height above the ground plane. Collective pitches of 10.1° and 15.1° were used in the comparison. For the low collective (10.1°), the measured thrust level gradually increases for the nondimensional rotor height, $G/D < 0.5$, as the rotor approaches the ground. For the high collective (15.1°), this characteristic is not shown in the measured data. As the rotor approaches the ground, the measured thrust level remains nearly constant. It is likely that the rotor was experiencing an increasing stall as the rotor approaches the ground, and the predicted thrust level disagrees with the measured data. The measured power level characteristics appear more complex. The measured power level decreases for the low collective as the rotor approaches the ground for $G/D < 0.5$, while it rises for the high collective. But, both the predicted power levels stay almost unchanged.

Figure 19 shows a breakdown of the predicted power level. As the rotor approaches the ground, its downwash decreases, which is caused by the ground blockage effect. As a result, the induced power level (C_{PI}/σ) decreases with less downwash. However, the reduced downwash increases the angle of attack, causing an increase in the profile power level (C_{PD}/σ). A sum of the induced and profile powers results in a total power, which stays almost flat.

Figure 20 shows a ratio of the in-ground effect (IGE) thrust and power to the OGE data with a rotor height variation. The low collective

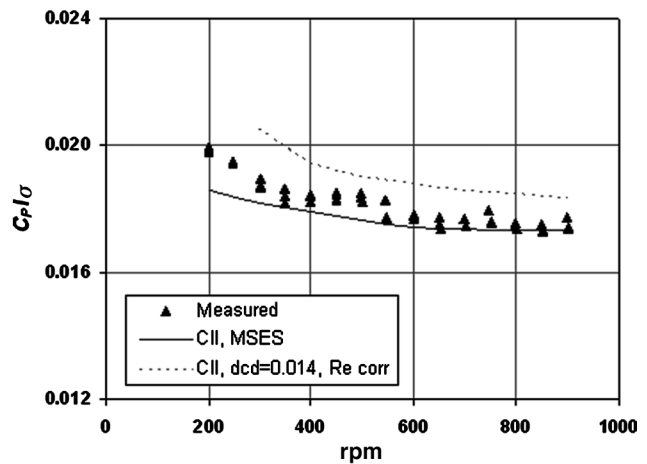


Fig. 17. Correlation of the thrust and power level with a rpm sweep for the AFDD single rotor ($\theta_{75} = 15.2^\circ$).

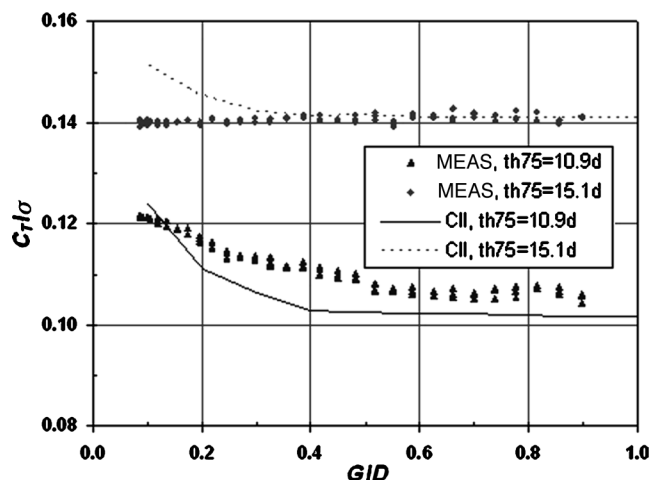


Fig. 18. Correlation of the thrust and power levels IGE for the AFDD single rotor with two different collective pitches.

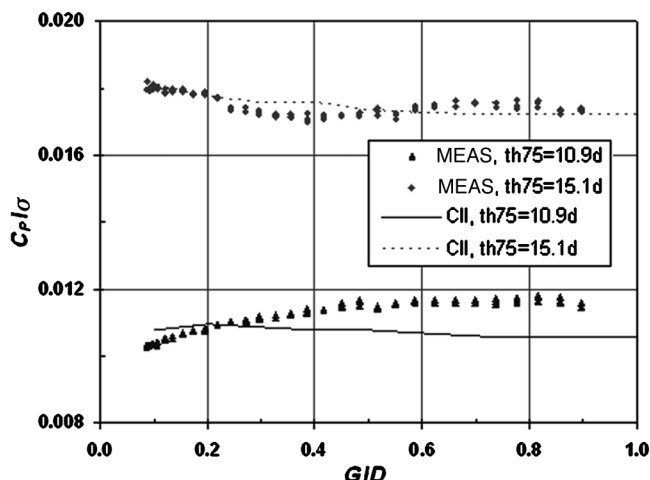


Fig. 19. A breakdown of the power level IGE for the low collective case.

result was used for the comparison, and the Lynx tail rotor test data (Ref. 30) were also included. The Lynx data were measured from the full-scale Lynx tail rotor test in the Outdoor Aerodynamic Research Facility (OARF) at NASA Ames Research Center. The IGE thrust is well predicted for the AFDD single rotor, and an approximate 10% gain of the IGE thrust from the OGE thrust is made at $G/D = 0.20$. The Lynx tail rotor test data show a similar trend as the AFDD data, though its thrust gain is higher. It was observed that the measured power decreases as the rotor approaches the ground, and a similar trend is shown in the Lynx tail rotor test data. However, the prediction fails to demonstrate a power decrease.

AFDD coaxial rotor performance

The upper and lower rotors of the AFDD coaxial were originally designed to be identical to each other. For a data quality check, a comparison of thrust and torque for the two rotors was made in Ref. 8 with a rpm sweep as shown in Fig. 21. This checking was made by letting the upper and lower rotors placed on their own test stand as an isolated rotor. The lower rotor was placed on the lower test stand, and the upper rotor was on the upper test stand. The collective pitch was 15.2° for the lower rotor (Run 316) and 15.1° for the upper rotor (Run 314). The lower

rotor was found to have a slight performance advantage over the upper rotor, although the results were within an expected variation.

Figure 22 provides a close-up view of the same figure in the neighborhood of 800 rpm, and the thrust and power data were shown in the nondimensionalized form for consistency with other comparisons. The variation of the measured thrust level (C_T/σ) and power level (C_P/σ) between the lower and upper rotors seems somewhat larger than expected. The largest variation between the two rotors is 0.0083 (equivalent to 1.2° collective difference) for the thrust level and 0.0009 (equivalent to 0.5° collective difference) for the power level, which implies that the two rotors are not exactly identical. The prediction using CAMRAD II is given by the line, and interestingly the predicted value is very close to the lower rotor measured data.

Rotor spacing effect. In a coaxial rotor configuration, the rotor height above the ground (G) is defined as the midpoint between two rotors, with the rotor spacing (S) defined as the separation distance between the two rotors. The measured torque is shown in Fig. 23 for both rotors, with the trimmed target used for the prediction. During the test, the rotor was trimmed to match the torques between the lower and upper rotors. In the test setup, the lower rotor was fixed at a distance of one diameter (D) above the ground plane, and the upper rotor translated vertically to achieve a range of the rotor spacing. Therefore, the rotor height (G/D) increased from 1.05 to 1.37 as the rotor spacing (S/D) varied from 0.1 to 0.8. The collectives were held fixed at 15.0° for the upper rotor, but varied from 14.6° to 15.1° for the lower rotor to match its torque with the upper rotor. The close-up view in Fig. 23 shows a significant increase in scattering of the measured power level for $S/D < 0.2$, where the largest scatter is found from the lower rotor data as $\Delta_{P,L} = 0.0014$ (equivalent to a 0.8° collective difference). The trim target for the prediction was calculated by the least-square method using the measured torque.

Figure 24 shows a comparison of the trimmed thrust level of both rotors between the measured and predicted data. In a coaxial rotor, the downwash at the lower rotor becomes larger than the upper rotor with an influence of the upper rotor wake. This would result in a lower thrust and a lower profile power for the lower rotor but a higher induced power. Note that the trimmed thrust of the lower rotor is substantially lower than that of the upper rotor.

As the rotor spacing decreases, the thrust gap between the two rotors decreases as found in the figure. The thrust level prediction for the upper rotor is consistently higher by 9% compared with the measured data. Taking into account a dissimilarity of the two rotors as seen in Fig. 22,

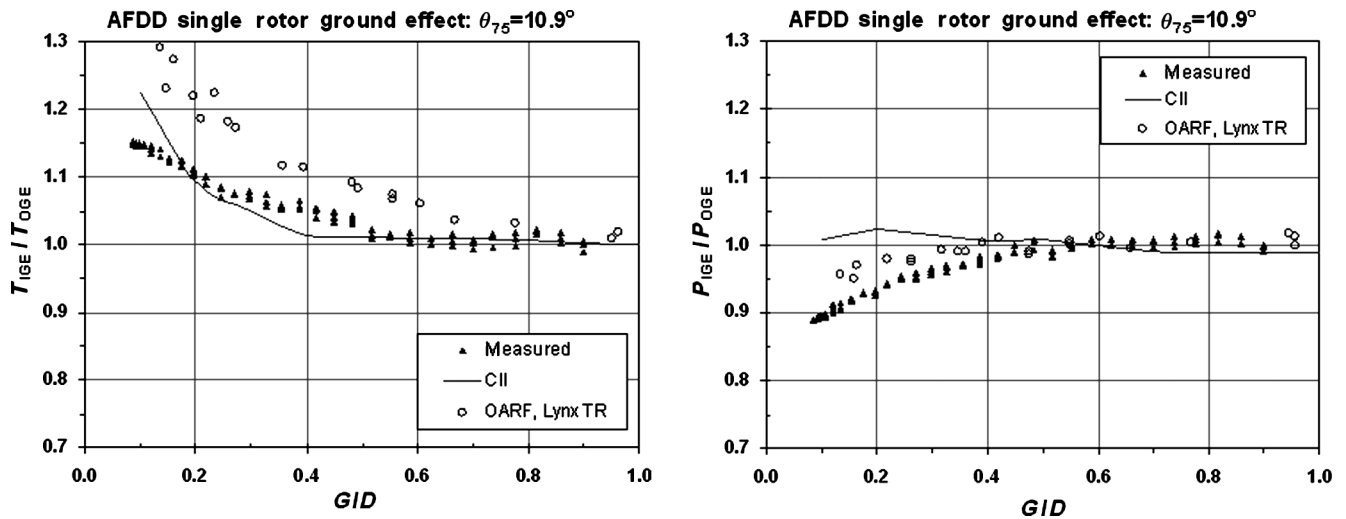


Fig. 20. Correlation of a ratio of the IGE thrust and IGE power for the AFDD single rotor.

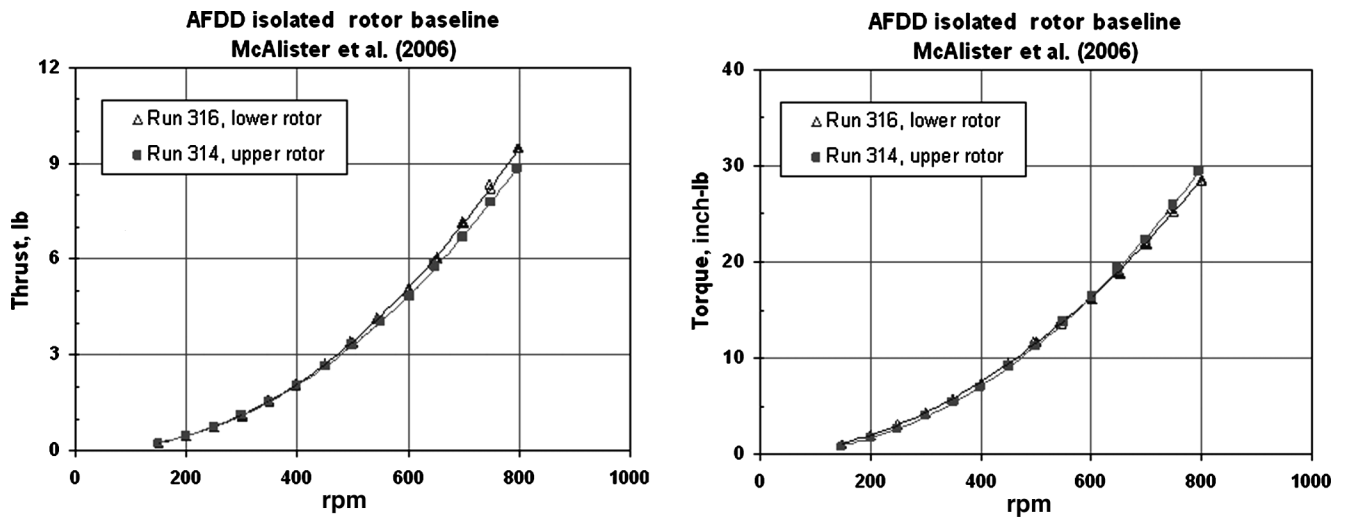


Fig. 21. Measured thrust and torque with a rpm sweep for the AFDD single rotor.

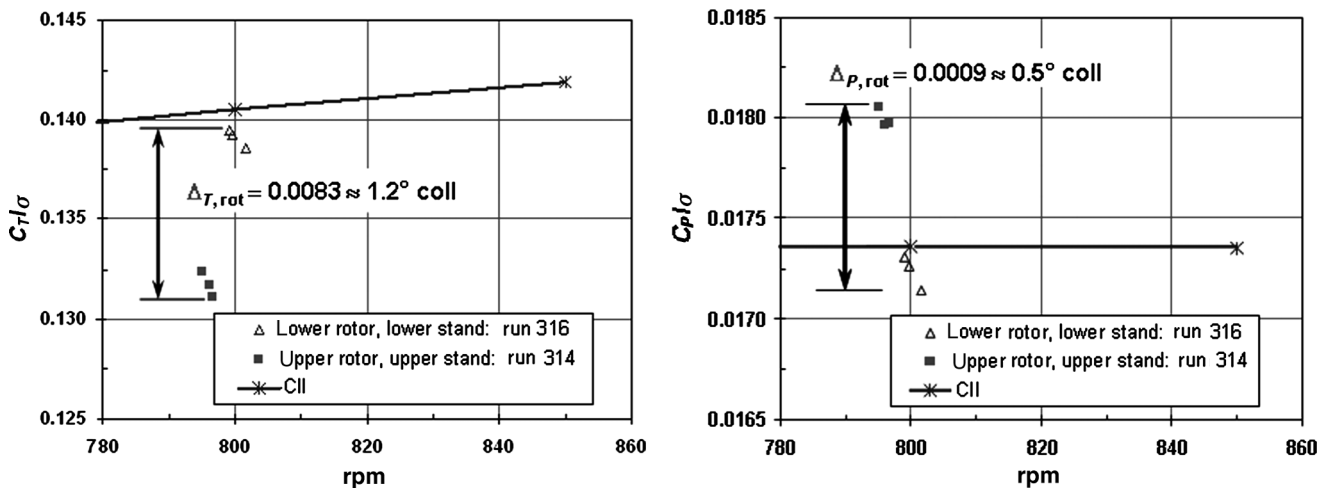


Fig. 22. A close-up of the thrust and power levels at 800 rpm for the AFDD single rotor.

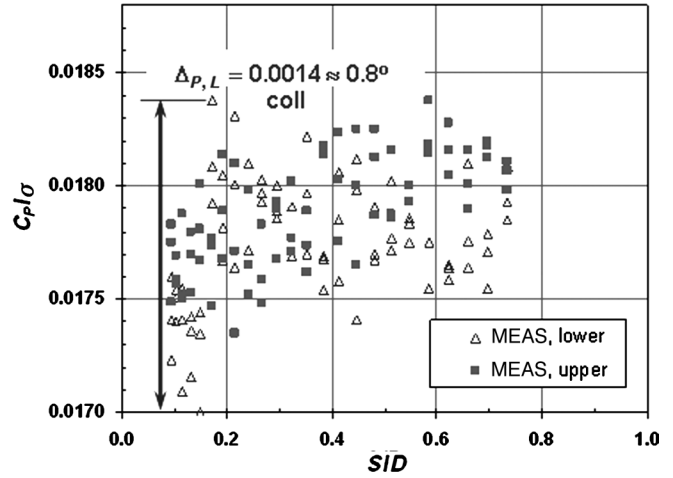
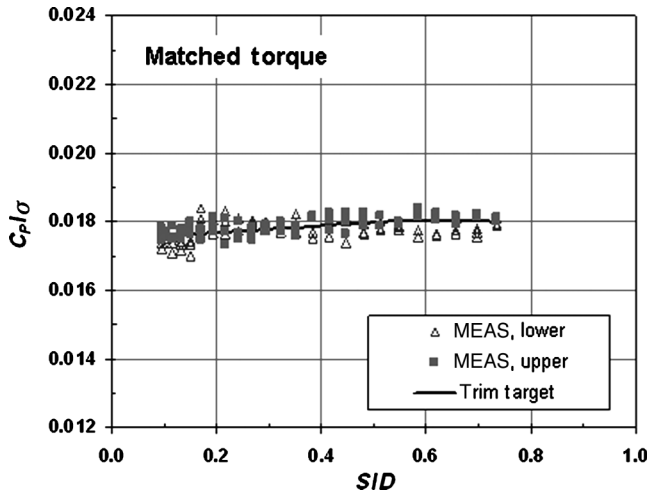


Fig. 23. Measured power level with a rotor spacing variation for the AFDD coaxial rotor.

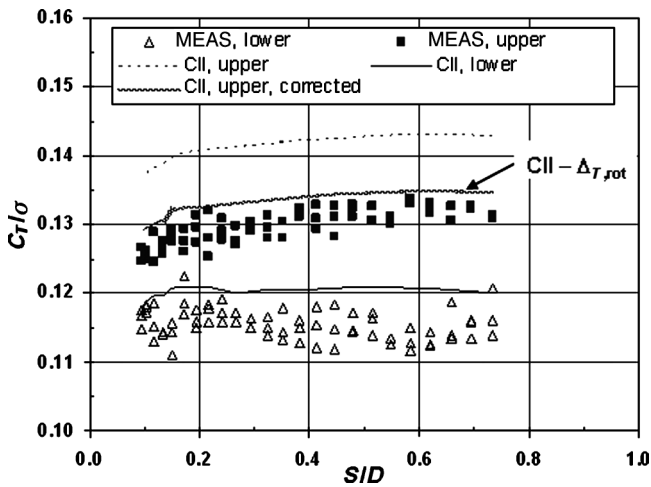


Fig. 24. Correlation of the trimmed thrust level with a rotor spacing variation for the AFDD coaxial rotor.

the corrected thrust level prediction for the upper rotor agrees better with the measured data.

Ground effect. In the ground effect test setup, a coaxial rotor translated vertically above the ground plane. Similar to the rotor spacing test, the two rotors were trimmed to match the torques at 800 rpm while the rotor spacing was fixed at $S/D = 0.1$. The collective was held fixed at 15.3° for the upper rotor, whereas it was varied from 14.2° to 15.5° for the lower rotor.

Figure 25 shows the measured power level of the two rotors and the trim target with a rotor height (G/D) variation. As the rotor height decreases for $G/D < 0.6$, the power required tends to rise, and there is approximately a 15% rise at $G/D = 0.1$ when translated from 0.8. This characteristic is unique and may result from the AFDD coaxial trim condition.

Figure 26 shows a comparison of the trimmed thrust level for both rotors. The measured thrust level of the lower rotor tends to rapidly rise as the G/D decreases, and the prediction agrees reasonably with the measured data. The measured thrust level of the upper rotor differs significantly from that of the lower rotor, in that it slowly increases as

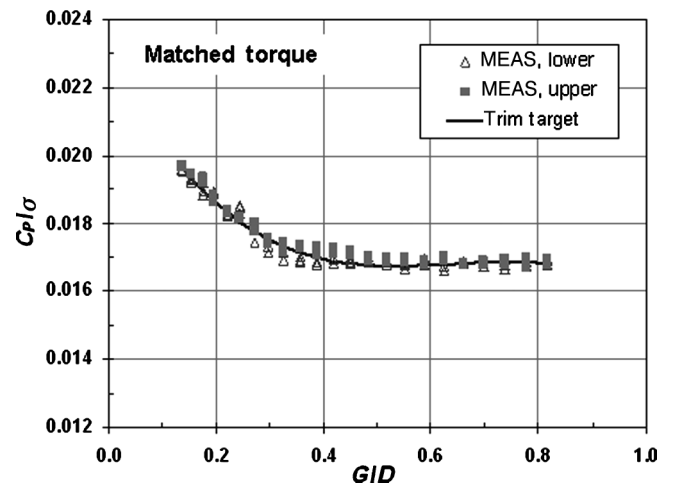


Fig. 25. Measured power level with a rotor ground height variation for the AFDD coaxial rotor.

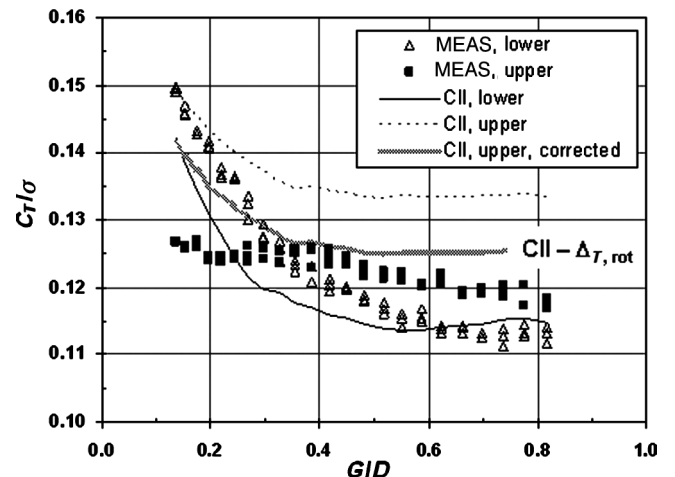


Fig. 26. Correlation of the trimmed thrust level with a rotor ground height variation for the AFDD coaxial rotor.

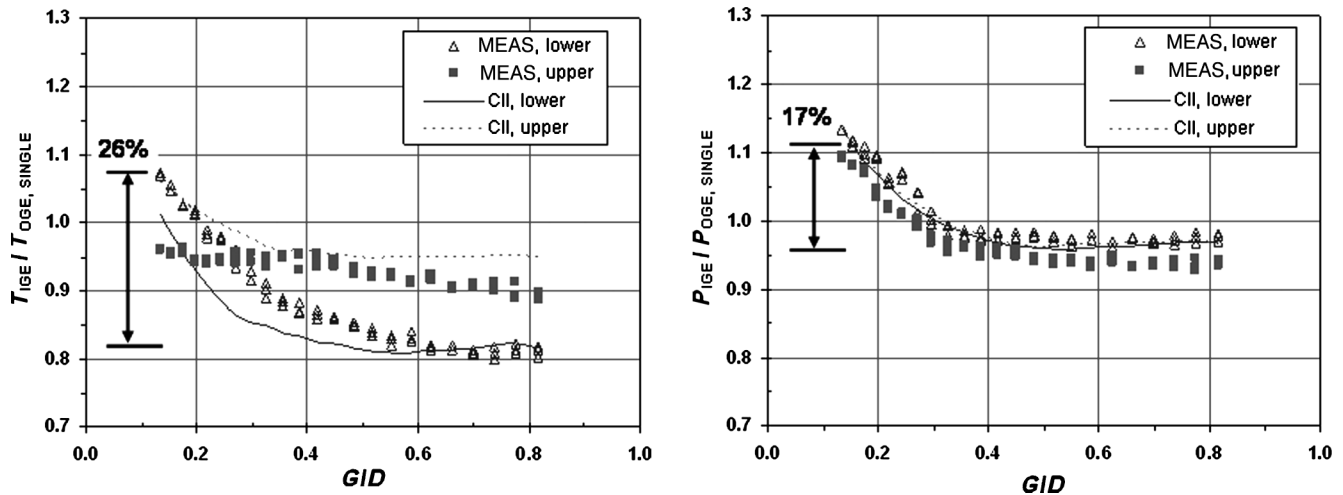


Fig. 27. Correlation of a ratio of the IGE thrust and IGE power with a rotor ground height variation for the AFDD coaxial rotor (referenced with the single rotor OGE data).

the G/D decreases. This is likely because the upper rotor experiences an increasing level of stall for $G/D < 0.4$. The predicted thrust level of the upper rotor fails to show the characteristics of the measured data, but a correction due to the dissimilarity of the two rotors improves the correlation.

Figure 27 shows a ratio of the AFDD coaxial IGE thrust and power to the single rotor OGE result with a rotor height (G/D) variation. The lower rotor of a coaxial loses more thrust than the upper rotor. In fact, it maintains only an 81% of the single rotor OGE thrust at $G/D = 0.8$, whereas the upper rotor achieves a 90% at the same rotor height. This more loss for the lower rotor may result from the coaxial rotor-to-rotor wake interference. The measured IGE thrust of the lower rotor rapidly rises as the G/D decreases. The lower rotor IGE thrust recovers by 26% from the OGE condition as the rotor height decreases from $G/D = 0.8$ –0.1. However, the upper rotor does not repeat this trend. The upper rotor IGE thrust slowly rises as the G/D decreases and recovers only by 6% as the rotor height decreases from $G/D = 0.8$ –0.4. For $G/D < 0.4$, the upper rotor IGE thrust remains almost unchanged.

The OGE power loss is measured an approximate 3% of the single rotor for the lower rotor and a 7% for the upper rotor. The IGE power recovers as the rotor height decreases. For $G/D < 0.3$, a rapid power recovery or even gain is found. The IGE power increases by approximately 17% as the G/D decreases from 0.8 to 0.1.

Conclusions

The hover performance data of full-scale and model-scale coaxial rotors have been compared with CAMRAD II prediction having a free vortex wake analysis. Performance correlations of a coaxial rotor were made with a variation of key parameters including the rotor spacing and height. To understand aerodynamic behavior of the AFDD coaxial rotor operating at a low Reynolds number, the Reynolds number scaling effect was explored using an airfoil design code, MSES. Overall, the performance prediction capability of a coaxial rotor is satisfactory compared with the measured data.

The following conclusions have been made from this study:

- 1) A free wake model enabled satisfactory performance correlation of the coaxial rotors. This conclusion was based on the correlation using the Harrington rotors, an XH-59A ABC rotor, and an AFDD coaxial rotor.
- 2) A rigorous exploration of the Reynolds number effect on a rotor operating at a low Reynolds number has led to the conclusion that

a simple Reynolds number correction could give an improvement of the performance prediction. The use of MSES-based airfoil tables was straightforward in methodology but significantly improved the correlation at low Reynolds numbers.

- 3) The measured thrust level of the AFDD single rotor decreased by 27% and the power level increased by 15% as the rotor speed reduced from 800 to 200 rpm. The low Reynolds number effect was captured well when using MSES-based airfoil tables.

- 4) The IGE thrust level of the AFDD single rotor was reasonably predicted for the low collective, but poorly predicted for the high collective. The IGE power level prediction failed to capture the trend of the measured IGE power for the low collective as the rotor height reduced.

- 5) The measured data indicated that the rotor spacing effect of the AFDD coaxial on the thrust appeared small, which was found consistently from the predicted results. The predicted upper rotor thrust was consistently higher by 9% compared with the lower rotor. The correction for upper rotor thrust due to a rotor dissimilarity improved performance correlation.

- 6) Owing to a coaxial rotor-to-rotor wake interference, the lower rotor of a coaxial maintained only an 81% of the single rotor OGE thrust, whereas the upper rotor achieved a 90%. As the rotor height decreased from $G/D = 0.8$ –0.1, the lower rotor IGE thrust recovered by 26% from the OGE condition, and the IGE power increased by 17%.

Acknowledgment

The authors would like to thank Mr. Ethan Romander, NASA Ames Research Center, for his help with MSES.

References

- ¹Hirschberg, M., "Sikorsky Pushes Forward with X2 Technology Demonstrator," *Vertiflite*, Vol. 51, No. 3, Fall 2005, p. 12.
- ²Bagai, A., "Aerodynamic Design of the X2 Technology Demonstrator™ Main Rotor Blade," American Helicopter Society 64th Annual Forum Proceedings, Montreal, Canada, April 29–May 1, 2008.
- ³Blackwell, R., and Millott, T., "Dynamics Design Characteristics of the Sikorsky X2 Technology™ Demonstrator Aircraft," American Helicopter Society 64th Annual Forum Proceedings, Montreal, Canada, April 29–May 1, 2008.

⁴Preator, R., Leishman, J. G., and Baldwin, G. D., "Performance and Trade Studies of Mono Tiltrotor Design," American Helicopter Society 61st Annual Forum Proceedings, Grapevine, TX, June 1–3, 2005.

⁵Cheney, M. C., Jr., "The ABC Helicopter," *Journal of the American Helicopter Society*, 14, (4), 1969, pp. 10–19.

⁶Arents, D. N., "An Assessment of the Hover Performance of the XH-59A Advancing Blade Concept Demonstration Helicopter," Report USAAMRD-L-TN-25, Eustis Directorate, USAAMRD, Fort Eustis, VA, May 1977.

⁷Burgess, R. K., "The ABC™ Rotor—A Historical Perspective," American Helicopter Society 60th Annual Forum Proceedings, Baltimore, MD, June 7–10, 2004.

⁸McAlister, K. W., Tung, C., Rand, O., Khromov, V., and Wilson, J. S., "Experimental and Numerical Study of a Model Coaxial Rotor," American Helicopter Society 62nd Annual Forum Proceedings, Phoenix, AZ, May 9–11, 2006.

⁹Coleman, C. P., "A Survey of Theoretical and Experimental Coaxial Rotor Aerodynamic Research," NASA TP 3675, 1997.

¹⁰Bagai, A., and Leishman, J. G., "Free-Wake Analysis of Tandem, Tilt-Rotor and Coaxial Rotor Configurations," *Journal of the American Helicopter Society*, 41, (3), 1996, pp. 196–207.

¹¹Wachspress, D. A., and Quackenbush, T. R., "Impact of Rotor Design on Coaxial Rotor Performance, Wake Geometry and Noise," American Helicopter Society 62nd Annual Forum Proceedings, Phoenix, AZ, May 9–11, 2006.

¹²Kim, H. W., and Brown, R. E., "Coaxial Rotor Performance and Wake Dynamics in Steady and Maneuvering Flight," American Helicopter Society 62nd Annual Forum Proceedings, Phoenix, AZ, May 9–11, 2006.

¹³Ruzicka, G. C., and Strawn, R. C., "Computational Fluid Dynamics Analysis of a Coaxial Rotor Using Overset Grids," Proceedings of the AHS Specialists' Conference on Aeromechanics, San Francisco, CA, January 23–25, 2008.

¹⁴Harrington, R. D., "Full-Scale-Tunnel Investigation of the Static-Thrust Performance of a Coaxial Helicopter Rotor," NACA TN 2318, 1951.

¹⁵Leishman, J. G., and Anathan, S., "Aerodynamic Optimization of a Coaxial Proprotor," American Helicopter Society 62nd Annual Forum Proceedings, Phoenix, AZ, May 9–11, 2006.

¹⁶Johnson, W. R., "CAMARD II, Vol II: Components Theory," Release 4.5, Johnson Aeronautics, Palo Alto, CA, 2006.

¹⁷Leishman, J. G., *Principles of Helicopter Aerodynamics*, Cambridge University Press, New York, NY, 2000.

¹⁸Squire, H. B., "The Growth of a Vortex in Turbulent Flow," *Aeronautical Quarterly*, Vol. 16, August 1965, pp. 302–306.

¹⁹Martin, P. B., "Measurement of the Trailing Vortex Formation, Structure, and Evolution in the Wake of a Hovering Rotor," Ph.D. Dissertation, University of Maryland, College Park, MD, 2001.

²⁰Bhagwat, M. J., "Transient Dynamics of Helicopter Rotor Wakes Using a Time-Accurate Free-Vortex Method," Ph.D. Dissertation, University of Maryland, College Park, MD, 2001.

²¹Leishman, J. G., and Bagai, A., "Challenges in Understanding the Vortex Dynamics of Helicopter Rotor Wakes," *AIAA Journal*, Vol. 36, (7), July 1998, pp. 1130–1140.

²²Felker, F. F., Betzina, M. D., and Signor, D. B., "Performance and Loads Data from a Hover Test of a Full-Scale XV-15 Rotor," NASA TM 86833, 1985.

²³Yamauchi, G. K., and Johnson, W., "Trends of Reynolds Number Effects on Two-Dimensional Airfoil Characteristics for Helicopter Rotor Analyses," NASA TM 84363, April 1983.

²⁴Drela, M., "A User's Guide to MSES 2.95," MIT Computational Aerospace Sciences Laboratory, September 1996.

²⁵Greer, D., Hamory, P., Krake, K., and Drela, M., "Design and Prediction for a High-Altitude (Low-Reynolds Number) Aerodynamic Flight Experiment," NASA TM-1999-206579, July 1999.

²⁶Selig, M. S., Donovan, J. F., and Fraser, D. B., *Airfoils at Low Speeds*, H. A. Stokely Publishing, Virginia Beach, VA, 1989.

²⁷Corrigan, J. J., and Schillings, J. J., "Empirical Model for Stall Delay Due to Rotation," American Helicopter Society Aeromechanics Specialists' Conference, San Francisco, CA, January 19–21, 1994.

²⁸Du, Z., and Selig, M. S., "A 3-D Stall-Delay Model for Horizontal Axis Wind Turbine Performance Prediction," AIAA 98-0021, January 1998.

²⁹Griffiths, D. A., and Leishman, J. G., "A Study of Dual-Rotor Interference and Ground Effect Using a Free-Vortex Wake Model," American Helicopter Society 58th Annual Forum Proceedings, Montreal, Canada, June 11–13, 2002.

³⁰Light, J. S., "Tip Vortex Geometry of a Hovering Helicopter Rotor in Ground Effect," American Helicopter Society 45th Annual Forum Proceedings, Boston, MA, May 22–24, 1989.